A Drosophila Tonic Motor Neuron Reinnervates Ectopic Muscles Fully Deprived of Native Tonic and Phasic Inputs

Lizzy Olsen[1,2,3], Parinita Mitchelle Mandhyan[1,2], Sara Arredondo[2], Komal Kaur[1,2], Ankura Sitaula[1,2], Aref Zarin[2,3*]

[1]Biology Graduate Program, Texas A&M University, College Station, United States

[2]Department of Biology, Texas A&M University, College Station, United States

[3]Texas A&M Institute for Neuroscience, Texas A&M University, College Station, United States

*For correspondence: azarin@bio.tamu.edu

Abstract

Motor neurons (MNs) form precise neuromuscular junctions (NMJs) during development, but the extent to which individual MNs can reinnervate fully denervated muscles in vivo remains poorly understood. In the Drosophila larva, each muscle is co-innervated by a tonic and a phasic glutamatergic MN. Here, we show that the tonic MN1 undergoes robust heterosynaptic sprouting and forms ectopic NMJs when neighboring muscles are deprived of both their native tonic and phasic inputs. This structural plasticity is not induced by silencing, but instead requires the physical ablation of adjacent MNs. Live imaging of the same MN1 axons in individual animals reveals that sprouting initiates early and expands progressively across larval stages. In contrast, phasic MNs show minimal remodeling, indicating that tonic MNs possess a greater intrinsic capacity for neuroplasticity. Notably, as MN1 establishes new synapses on targets it does not normally innervate, it redistributes pre-synaptic territory across both native and ectopic muscles. These findings identify a subtype-specific, injury-induced rewiring program in an intact motor circuit.

Introduction

Spinal cord injury, stroke, and neurodegenerative disease disrupt neural circuits, impairing motor and cognitive function. Functional recovery may depend on heterosynaptic structural plasticity (HTSP), in which intact neurons sprout new branches to reinnervate denervated targets (1-3).

Therapeutic strategies aimed at enhancing HTSP hold promise, but their success hinges on a deeper understanding of the intrinsic and extrinsic factors that promote or constrain neuronal sprouting (4). Neurons differ in properties such as firing dynamics (e.g., tonic versus phasic), neurotransmitter identity, and synaptic architecture (e.g., large versus small boutons), but it remains unclear whether all neuron types are equally capable of structural remodeling after injury. This gap limits our ability to predict which neurons can compensate for lost inputs—and under what conditions. A central question, therefore, is how physiologically distinct neurons respond to the dysfunction or loss of their synaptic partners. Here, we examine the capacity for post-injury axonal sprouting and neuromuscular junction (NMJ) remodeling in physiologically distinct tonic and phasic motor neurons in Drosophila larvae.

The *Drosophila* larval neuromuscular system provides a genetically accessible and anatomically tractable model for investigating neuron subtype-specific injury responses. Larval muscles are innervated by two classes of glutamatergic excitatory motor neurons (MNs): tonic-firing type Ib MNs, which form large boutons and typically innervate a single muscle, and phasic-firing type Is MNs, which form smaller boutons and innervate multiple muscles (5-12). These MNs converge on shared target muscles, creating a synaptic motif in which one tonic and one phasic MN co-innervate the same postsynaptic muscle fiber. This configuration provides a unique opportunity to directly compare how distinct MN subtypes respond to the same insult. Notably, convergence of tonic and phasic inputs onto a common postsynaptic cell is an evolutionarily conserved circuit motif observed across both vertebrate and invertebrate systems (13-16). Due to its simplicity and powerful genetic toolkit, the *Drosophila* NMJ has long served as a leading model for dissecting conserved mechanisms of synaptic development and plasticity at single-cell resolution (5, 6, 8, 10, 17-29).

Previous studies have shown that ablating—but not silencing—the phasic MN RP2 induces structural expansion of the NMJ formed by its co-innervating tonic partner MN1 on Muscle 1, while loss of MN1 has no effect on RP2 (7-10). These findings suggest that tonic MNs are more structurally adaptive than phasic MNs. However, since only one MN type was disrupted in those studies, the muscles retained partial excitatory input. Thus, whether complete denervation prompts more robust or qualitatively different plastic responses—and which neurons are capable of compensating—remains unknown.

To address this, we developed a genetic paradigm to simultaneously ablate both tonic and phasic MNs that co-innervate dorsal longitudinal muscles, creating a fully denervated group of target muscles. We found that the surviving tonic MN1, which normally innervates Muscle 1, exhibited robust axonal sprouting and formed ectopic NMJs on denervated muscles it does not typically target. In contrast, the phasic MN RP2 did not sprout following ablation of its tonic partners, and MN1 failed to sprout when neighboring MNs were chronically or acutely silenced rather than ablated. These results demonstrate that injury-induced HTSP is neuron-subtype specific and requires complete physical loss of input—not merely loss of activity—to initiate structural remodeling.

We further show that the ectopic NMJs formed by MN1 are functional: they restore calcium transients in previously denervated muscles and partially rescue crawling performance. Using live motor axon imaging, behavioral assays, and temporally controlled genetic ablation, we mapped the dynamics of MN1 sprouting across larval stages. Sprouting was initiated shortly after larval hatching and continued throughout larval development, revealing a broader plasticity window than previously appreciated.

Together, our findings identify a MN subtype-specific and injury-dependent form of HTSP that enables functional circuit compensation. This work uncovers key cellular and temporal principles governing adaptive circuit remodeling and provides a foundation for understanding how defined neurons sense local denervation and initiate compensatory growth programs.

Results

Tonic MN1 Sprouts and Forms Ectopic NMJs Following Complete Denervation of Neighboring Muscles

The *Drosophila* larval body comprises three thoracic segments (T1–T3) and nine abdominal segments (A1–A9). The central nervous system (CNS) consists of two brain lobes and a segmented ventral nerve cord (VNC), which functions analogously to the vertebrate spinal cord. Each VNC segment controls the muscles of its corresponding

body segment (**Fig. 1A**). In each abdominal segment, approximately 30 bilaterally symmetrical muscle pairs are innervated by 28 pairs of tonic and two pairs of phasic glutamatergic excitatory motor neurons (MNs) projecting from the segmental VNC (5, 30-36) (**Fig. 1A**).

In this study, we focused on the dorsal-longitudinal (DL) muscles, specifically Muscles 1, 2, 9, and 10 (**Fig. 1A**). These muscles receive inputs from a common phasic-firing MN-Is, also known as RP2 or the common dorsal excitor (CDE), and four distinct tonic-firing (Ib) MNs—MN1, MN2, MN9, and MN10—each innervating an individual muscle (**Fig. 1A**) (5, 30-36).

Previous studies have shown that apoptotic ablation of the phasic MN-Is (hereafter referred to as **Is**) leads to structural expansion of the neuromuscular junction (NMJ) formed by the co-innervating tonic MN1, increasing tonic input to Muscle 1. In contrast, ablation of the tonic MN1 does not trigger structural changes in the NMJ formed by MN-Is (7-10). These findings highlight intrinsic differences in how tonic and phasic MNs respond to the loss of their co-innervating partners. However, these studies removed only one MN class—either tonic or phasic—leaving the target muscles partially innervated. Thus, it remained unclear whether complete removal of both excitatory inputs could trigger compensatory sprouting by other MNs.

To address this, we genetically ablated either or both tonic and phasic MNs innervating Muscles 2, 9, and 10 and examined structural remodeling by the bystander MN1 (**Fig. 1B–D**). For ablation, we used previously validated MN-LexA drivers (37, 38) to express the pro-apoptotic genes *reaper (rpr)* and *head involution defective (hid)*, inducing cell death in targeted MNs (39). The tonic MN1 was visualized using 94G06 (40) (MN1 Ib)-Gal4 driving UAS-myr-GFP.

We found that MN1 did not form ectopic NMJs when only the phasic MN-Is was ablated (Is >RPR) and only formed ectopic NMJs on Muscle 2 when tonic MNs 2, 9, and 10 were ablated (CQ >RPR) (**Fig. 1 D,E**). In contrast, concurrent ablation of both tonic and phasic

121 MNs (CQ ∪ Is > RPR) triggered robust sprouting of MN1, which extended axons and
122 formed de novo NMJs on fully denervated Muscles 2, 9, and 10 (**Fig. 1 D,E**).

123 Quantitative morphometric analysis (41, 42) (**Fig. 1 C)** revealed that MN1 in CQ ∪ Is
124 >RPR larvae showed a significant increase in overall NMJ area across all four DL
125 muscles (1, 2, 9, and 10) compared to controls, while average bouton size and total
126 bouton number remained unchanged (**Fig. 1 D,E**). Importantly, the total MN1 NMJ area
127 was redistributed across the DL muscles, with reduced allocation to its native target
128 Muscle 1 compared to controls—suggesting an upper limit on the total synaptic area
129 MN1 can establish (**Fig. 1 D,E**). Finally, we quantified total axonal and NMJ branch
130 points. CQ > RPR and CQ ∪ Is > RPR larvae showed a significant increase in axon
131 branch points (GFP-only), consistent with a sprouting phenotype, whereas NMJ branch
132 points (Dlg+GFP) were not significantly altered (**Fig. 1 D,E**).

133 Together, these results demonstrate that robust heterosynaptic sprouting of MN1 is
134 selectively triggered by complete loss of both tonic and phasic excitatory inputs to
135 neighboring muscles.

136

137

138 **Phasic MN-Is Maintains Its Normal Innervation After Ablation of Co-innervating**
139 **Tonic MNs**

140 Our earlier experiments demonstrated that the tonic MN1 exhibits robust heterosynaptic
141 sprouting when neighboring muscles are fully deprived of both tonic and phasic inputs.
142 We next asked whether the phasic MN-Is possesses a comparable capacity for structural
143 remodeling and NMJ expansion following the loss of its tonic co-innervators.

144

145 Previous studies, in which only MN1 was ablated, reported no structural changes in
146 NMJs formed by the phasic MN-Is on Muscle 1 (7-10). To extend these findings, we
147 ablated additional tonic MNs (MN1, MN2, MN9, and MN10), thereby fully depriving the
148 dorsal-longitudinal (DL) muscles 1, 2, 9, and 10 of all tonic innervations (**Fig. 2A**). In
149 both control and ablated groups, the phasic MN-Is was visualized using myr-GFP driven

150 by an enhancer element cloned from the 27E09-Gal4 driver, which selectively targets
151 phasic MNs.

152 Following tonic MN ablation (CQ ∪ MN1 >RPR), the intact phasic MN-Is retained its
153 normal innervation pattern on Muscles 1, 2, 9, and 10 (**Fig. 2A**). Apart from a modest
154 reduction in the number of 2nd- and 3rd-order axonal branches in CQ ∪ MN1 >RPR
155 larvae, there were no significant differences in bouton number, area, or size between
156 control and ablated groups (**Fig. 2B, C**). Despite complete loss of tonic excitatory input,
157 the phasic MN-Is did not exhibit ectopic sprouting or NMJ expansion on these muscles.

158 This lack of response contrasts sharply with the extensive sprouting observed in MN1
159 under similar conditions, underscoring a fundamental difference in the plasticity potential
160 of tonic versus phasic MNs. Consistent with earlier studies (7-10), these results suggest
161 that phasic MN-Is lacks the intrinsic capacity for compensatory structural remodeling
162 following the loss of its co-innervating tonic partners.

163

164

165 **MN1 Sprouting is Induced by Ablation but Not by Chronic or Acute Silencing of**
166 **Neighboring MNs**

167 To confirm that the robust sprouting observed in MN1 results specifically from the loss
168 of neighboring motor neurons—and not from artifacts of the LexA/AOP genetic
169 system—we repeated the ablation experiments using the Gal80^{ts}/GAL4/UAS system.
170 Gal80^{ts} inhibits GAL4 activity at 24°C but not at 29°C (43, 44).

171 Using previously characterized CQ and Is GAL4 drivers (7, 36-38, 40, 45), we targeted
172 the tonic MN2, MN9, and MN10 along with the phasic MN-Is for UAS-reaper (rpr)-
173 mediated ablation. MN1 was labeled with MN1-lexA >AOP-myr-GFP. Animals raised
174 continuously at 29°C showed robust MN1 sprouting and ectopic NMJs on denervated
175 Muscles 2, 9, and 10, whereas controls maintained at 24°C (with functional Gal80 protein
176 blocking GAL4 activity) showed no sprouting (**Fig. 3A-B, Supp Fig S1**). These findings

177 confirm that MN1 sprouting is specifically triggered by the physical loss of neighboring
178 MNs rather than by potential genetic artifacts.

179 We next tested whether silencing the activity of neighboring MNs—without their
180 physical removal—would be sufficient to induce MN1 sprouting. For acute silencing, we
181 used the light-activated chloride channel GtACR1, which causes chloride influx and
182 neuronal hyperpolarization upon light exposure (46, 47). Previous works have
183 demonstrated the efficacy of GtACR1 in silencing MNs and other neurons in Drosophila
184 larvae (37, 45, 48, 49). In CQ ∪ Is >GtACR1 larvae, MN1 maintained its normal
185 innervation of Muscle 1 and did not form ectopic NMJs on Muscles 2, 9, or 10. However,
186 we observed a modest increase in MN1 NMJ area and bouton number compared to
187 controls, without changes in bouton size (**Fig. 3A-B, Supp Fig S1**).

188 We then tested chronic silencing using botulinum neurotoxin-C (BoNT-C), which blocks
189 both evoked and spontaneous neurotransmitter release (27, 28). In CQ ∪ Is >BoNT-C
190 larvae, MN1 did not form ectopic NMJs, but the number of boutons on Muscle 1 was
191 significantly increased relative to controls, despite no changes in NMJ area or bouton
192 size. (**Fig. 3A-B Supp Fig S1**).

193 We then expressed tetanus toxin light chain (TeTxLC), which blocks evoked but not
194 spontaneous neurotransmitter release (50). In CQ ∪ Is >TeTxLC larvae, MN1 again did
195 not form ectopic NMJs, but showed substantial NMJ expansion on its native target,
196 Muscle 1 (**Fig 3 A-C Supp Fig S1**). This included significantly increased NMJ area,
197 branching, and bouton number, along with a marked reduction in average bouton size
198 (**Fig 3 B-C Supp Fig S1**). These features are consistent with satellite bouton formation
199 previously observed following TeTxLC-mediated silencing of MN-Is (7, 8). Notably, Dlg
200 staining revealed that the NMJs of TeTxLC-silenced tonic MNs maintained normal
201 morphology and did not exhibit the extensive NMJ overgrowth observed in the bystander
202 MN1 (**Fig. 3A)**, suggesting that the sprouting phenotype is specific to the unaffected
203 neuron responding to loss of presynaptic activity in neighboring inputs.

204 Taken together, these results demonstrate that heterosynaptic sprouting of MN1 requires
205 the physical ablation of neighboring MNs. In contrast, silencing of neighboring MNs—
206 whether acute or chronic—does not trigger ectopic sprouting, though it can modulate
207 bouton number and NMJ structure at the native target.
208

209 **Ectopic MN1 Sprouting Restores Muscle Activation and Partially Rescues Crawling**
210 **Behavior**

211 Thus far, we have shown that concurrent ablation—but not silencing—of neighboring
212 tonic and phasic MNs triggers robust sprouting of the bystander MN1, resulting in
213 ectopic NMJs on fully denervated Muscles 2, 9, and 10. To determine whether these
214 ectopic NMJs are functional and capable of activating the muscles they innervate, we
215 performed in vivo muscle calcium imaging in intact, forward-crawling larvae.

216 As a baseline, we first examined muscle calcium activity in larvae where all tonic and
217 phasic MNs innervating dorsal muscles 1, 2, 9, and 10 were either genetically ablated
218 (CQ-lexA, 27E09-lexA; 94G06-lexA >RPR) or acutely silenced (CQ-lexA, 27E09-lexA;
219 94G06-lexA >GtACR1) (**Fig 4 A-C**). In both groups, the dorsal-longitudinal (DL)
220 muscles failed to show calcium transients or contraction during forward crawling,
221 confirming complete loss of excitatory input. In contrast, ventral and lateral muscles with
222 intact MN innervation exhibited robust calcium activity and contractions (**Fig 4 A,B;**
223 **Video S1, Video S2, Video S3**). These observations validate that (i) both GtACR1-
224 mediated silencing and RPR-mediated ablation effectively eliminate MN output and (ii)
225 the MN driver lines selectively target the intended MNs without affecting off-target MNs.

226 We then repeated these experiments but spared MN1. In the acute silencing group (CQ-
227 lexA, 27E09-lexA >GtACR1), only Muscle 1 displayed calcium transients and
228 contraction during crawling, consistent with MN1 maintaining its normal innervation
229 (**Fig 4 A,B; Video S4**). By contrast, in the ablation group (CQ-lexA, 27E09-lexA
230 >RPR), all four dorsal muscles (1, 2, 9, and 10) exhibited calcium transients and
231 contraction, demonstrating that ectopic NMJs formed by MN1 are capable of restoring
232 contractile activity in denervated muscles (**Fig 4 A,B; Video S5**).

233 To directly test whether the sprouted MN1 drives these responses, we acutely silenced
234 MN1 (94G06-Gal4 >GtACR1) in larvae where neighboring MNs had been ablated (CQ-
235 lexA, 27E09-lexA >RPR). Silencing MN1 abolished calcium activity in all four dorsal
236 muscles during crawling, confirming that the sprouted MN1 terminals are functionally
237 active and required for muscle contraction (**Fig 4 A,B; Video S6**).

238 Next, we investigated whether MN1 sprouting contributes to behavioral recovery. We
239 quantified forward crawling by measuring peristalsis efficiency (distance traveled per
240 peristalsis) and peristalsis duration (time to complete a forward wave). Control larvae
241 displayed a peristalsis efficiency of ~0.8 mm per wave. Larvae lacking dorsal MN inputs
242 (CQ-lexA, 27E09-lexA; 94G06-lexA >RPR) showed markedly reduced efficiency, but
243 those with intact MN1 (CQ-lexA, 27E09-lexA >RPR) performed significantly better,
244 indicating partial restoration of crawling (**Fig 4 D,E; Video S7**).

245 Notably, CQ-lexA, 27E09-lexA >RPR larvae also outperformed CQ-lexA, 27E09-lexA
246 >GtACR1 larvae (**Fig 4 D,E; Video S7**), suggesting that ablation-induced sprouting of
247 MN1 (occurring in the ablated group but not in the silenced group) underlies this
248 improvement. However, because 27E09-lexA also targets ventral-projecting phasic MNs,
249 it is possible that structural plasticity of ventral tonic MNs contributed to recovery. To
250 isolate MN1's contribution, we silenced the sprouted MN1 in CQ-lexA, 27E09-lexA
251 >RPR larvae using 94G06-Gal4 >GtACR1. This manipulation significantly reduced
252 peristalsis efficiency compared to unsilenced CQ-lexA, 27E09-lexA >RPR larvae (**Fig 4**
253 **D,E; Video S7**), directly demonstrating that MN1 sprouting is adaptive and improves
254 locomotion.

255 Across all genotypes, we observed an inverse relationship between peristalsis efficiency
256 and peristalsis duration: larvae traveling shorter distances per peristaltic wave also
257 exhibited slower propagation of contractions across body segments, resulting in longer
258 peristalsis durations (**Fig 4 E; Video S7**).

259 Together, these results establish that MN1 ectopic sprouting restores muscle contractility
260 and partially rescues motor behavior, highlighting its role as a compensatory response
261 following injury.

262

263 Ectopic MN1 Sprouting Occurs Primarily During Larval Stages

264 In *Drosophila*, embryogenesis lasts ~22–24 hours at 25°C, after which the embryo
265 hatches into a first instar larva (L1) capable of foraging, feeding, and performing
266 locomotor behaviors such as forward crawling. By hatching, core motor circuits are
267 already established, with motor neurons forming functional synapses onto their target
268 muscles. The L1 stage lasts ~25 hours, followed by molting into second (L2) and third
269 instar (L3) stages, each lasting ~24–25 hours before pupation. Our initial analyses of
270 MN1 sprouting and ectopic NMJ formation were performed in L3 larvae. To better define
271 the timeline of these structural changes, we examined MN1 remodeling across the L1–L3
272 transition in animals with ablated tonic and phasic MNs.

273 Using live imaging of MN1 labeled with tdTomato, we tracked axonal branching in
274 individual larvae at L1, L2, and L3 stages. Between imaging sessions, larvae were
275 recovered and returned to food to continue development. This allowed us to quantify and
276 distinguish 1st-, 2nd-, and 3rd-order axon branches extending from MN1's main shaft
277 (**Fig. 5A schematic**).

278 At L1, MN1 axons in ablated larvae already exhibited a twofold increase in 1st-order
279 branches compared to controls, while 2nd-order branching was comparable between
280 groups. By L3, ablated larvae showed significantly higher numbers of 1st-order branches
281 relative to controls. Within the ablated group, both 1st- and 2nd-order branch numbers
282 increased significantly from L1 to L3, whereas in controls only 2nd-order branching
283 increased across development. These findings suggest that while MN1 sprouting in
284 ablated animals is initiated early, the majority of axon branching and ectopic NMJ
285 formation occurs progressively during the L1–L3 transition **(Fig. 5A–B; Supp. Fig.)**.

286 To test whether MN1 sprouting can be induced exclusively during larval stages, we
287 performed temporally restricted ablation. Since MN-Gal4 drivers (e.g., CQ-Gal4, 27E09-
288 Gal4) activate UAS-rpr/hid from embryogenesis onward, we used Gal80^{ts} to suppress
289 Gal4 activity at 24°C and permit it at 29°C (43, 44). For larval-only ablation, embryos
290 were maintained at 24°C until hatching and then shifted to 29°C from L1 through L3
291 prior to NMJ analysis. As reference points, we used data from embryonic ablation
292 (continuous 29°C) and control animals (continuous 24°C) described earlier in **Fig. 3**.
293 Larvae subjected to larval-stage ablation showed MN1 sprouting and ectopic NMJ
294 formation, though to a lesser extent than embryonically ablated animals (**Fig. 5C–D**).

295 Taken together, these results indicate that MN1 sprouting is initiated early but progresses
296 substantially throughout larval development, with the L1–L3 period representing a key
297 window for ectopic NMJ formation following injury.

298
299

300 Discussion

301 **Subtype-Specific Plasticity Revealed Through Complete Denervation**

302 Our study reveals a robust, subtype-specific capacity for structural plasticity within an established
303 motor circuit following injury. We demonstrate that tonic MN1, but not phasic MN-Is, undergoes
304 extensive axonal sprouting and ectopic NMJ formation when neighboring tonic and phasic MNs
305 are ablated. These ectopic NMJs restore muscle contractility and contribute to improved
306 locomotor performance, providing functional evidence that the observed plasticity is adaptive. In
307 contrast, when neighboring MNs are functionally silenced without ablation, MN1 does not sprout,
308 indicating that complete physical loss—not merely loss of synaptic activity—is required to trigger
309 heterosynaptic structural plasticity (HTSP).
310

311 Our approach builds on earlier observations by Chang and Keshishian (1996), who reported that
312 embryonic denervation could lead to some ectopic innervation from nearby neurons (51).
313 However, they utilized laser-mediated MN ablation, which resulted in variable levels of
314 denervation and often lacked control over which neurons contributed to reinnervation. In contrast,
315 we used targeted genetic ablation to achieve reproducible, complete denervation of specific
316 muscles, revealing that sprouting arises specifically from the identified tonic MN1. Furthermore,

317 we show that the newly formed NMJs are functional and that sprouting mainly occurs after larval
318 hatching and continues across larval stages, defining a broader temporal window for plasticity.
319
320 In more recent studies investigating NMJ plasticity, either tonic or phasic MNs were disrupted,
321 but never both. As a result, target muscles continued to receive partial excitatory input from
322 surviving MNs, allowing for homeostatic compensatory changes within an already innervated
323 context. Thus, the effects of completely removing all excitatory input from a given muscle and
324 testing whether other MNs can sprout to reinnervate these fully denervated targets remained
325 unknown. To address this gap, we developed genetic tools enabling the simultaneous ablation of
326 both tonic and phasic MNs innervating specific muscles, creating a fully denervated environment.
327 This strategy revealed a previously unrecognized capacity for bystander MN1 to form de novo
328 ectopic NMJs and reestablish motor output. This subtype specificity aligns with prior findings
329 that tonic Ib MNs—but not phasic Is MNs—exhibit structural and functional compensation
330 following input loss (7, 8, 10). Our findings extend this framework by demonstrating that MN1
331 can not only expand existing synaptic terminals but also innervate novel postsynaptic targets,
332 forming functional ectopic NMJs on muscles it does not typically contact. This level of
333 remodeling goes beyond classic homeostatic plasticity and reflects a more profound form of
334 structural reorganization.
335
336 Importantly, MN1 sprouting occurred only following the physical ablation of neighboring MNs
337 and not when those MNs were chronically or acutely silenced. Our findings further support that
338 tonic MNs possess a greater intrinsic capacity for structural remodeling in response to injury
339 compared to phasic MNs. This finding agrees with Han et al. (2022), who showed that botulinum
340 toxin silencing—even when eliminating both evoked and spontaneous transmission—does not
341 induce structural compensation, whereas physical loss does (27). These results emphasize that
342 circuit rewiring is not merely a response to inactivity but likely requires injury-associated cues
343 such as axonal degeneration or glial signaling.
344
345 Our injury model appears to diverge from CNS critical period constraints. Ackerman et al. (2021)
346 silenced MN1 and MN-Is and examined dendritic remodeling within the same MNs, identifying
347 an early embryonic window during which activity loss induces dendritic growth (52). In contrast,
348 we demonstrate that MN1 can undergo peripheral axonal remodeling beginning 0–4 h after larval
349 hatching and continuing throughout larval stages, highlighting that different compartments of the
350 same neuron (dendrites vs. axons) follow distinct temporal rules for plasticity.

351

352 **Intrinsic Differences in Plasticity Between Tonic MN1 and Phasic MNs**

353

354 MN1 displays a markedly greater intrinsic capacity for structural plasticity compared to its phasic
355 counterparts, such as the phasic MN-Is. This enhanced plasticity is likely underpinned by a
356 multilayered set of molecular, structural, genetic, and functional differences at the synaptic,
357 transcriptional, and cellular level (28, 38, 53, 54).

358

359 Structurally, tonic MN1 forms larger synaptic boutons with expansive, donut-shaped
360 active zones and a 4.4-fold larger neuromuscular junction area at muscle 1 containing
361 3.8-fold more active zones (AZ), creating an ideal substrate for growth and remodeling,
362 unlike the compact active zones of phasic neurons optimized for rapid transmission rather
363 than plasticity (13, 27, 28, 38, 54). Functionally, tonic MN1 displays lower basal synaptic
364 output and more "silent" active zones possibly conducive to sprouting, whereas phasic
365 MN-Is show high initial release probability (Pr) that depresses with repetitive stimulation
366 (54). Importantly, high-Pr phasic MN-Is synapses show denser voltage-gated calcium channel
367 (VGCC) clustering and tighter **vesicle** coupling—architectural features that could enhance
368 release efficiency but may potentially constrain structural remodeling and growth (54).

369

370 At the molecular level, MN1 expresses significantly elevated levels of growth-promoting genes
371 including Wnt4 (40-fold higher), Pyramus, Toll-6, and SiaT—establishing a growth-permissive
372 transcriptional program and environment (38). Conversely, phasic neurons upregulate calcium
373 buffering proteins like Cbp53E (30-fold higher) and vesicle trafficking chaperones that constrain
374 remodeling (38). MN1's superior calcium handling—maintaining higher resting calcium levels
375 while enabling rapid extrusion after activity—prevents growth inhibition and supports sprouting,
376 unlike phasic neurons that accumulate excessive calcium during stimulation with slower
377 recovery. Furthermore, MN1's distinct post-translational modifications, cytoskeletal regulation,
378 and broader distribution of scaffolding proteins like Bruchpilot could likely create a cellular
379 environment permissive to structural reorganization and functional recovery after injury,
380 fundamentally distinguishing it from phasic neurons that are intrinsically optimized for high-
381 fidelity transmission rather than adaptive structural change.

382

383 **Evolutionary Parallels in Injury-Induced Plasticity**

Our findings reflect a conserved strategy for injury-induced plasticity across species. In the mammalian spinal cord, both interneurons and descending corticospinal tract (CST) neurons can sprout following injury, particularly when targets are fully or partially denervated (55). Similar to our findings in Drosophila, this rewiring often originates from spared neurons, such as CST axons that form new connections post-lesion (56, 57). Notably, Nakamura et al. showed that collateral sprouting from spared CST axons—rather than long-distance regeneration of damaged neurons—was sufficient to restore motor control (57), echoing our demonstration that MN1 can reinnervate denervated targets to restore crawling.

Additional studies highlight that promoting plasticity, not just regeneration, may be key for functional recovery (58, 59). These studies emphasize the role of the injury environment, including target denervation and glial modulation, in supporting sprouting (60, 61). Vertebrate work shows that denervated muscle and Schwann cells transiently emit growth-permissive cues that support reinnervation (62). Brown and Holland (1979) demonstrated that partial denervation of mouse soleus muscle triggers sprouting from intact motor axons, and that this response is suppressed by direct electrical stimulation of denervated muscle—indicating that specific signals from denervated targets, not simply inactivity, drive structural plasticity (63). Keynes et al. (1983) further confirmed that structurally intact, but denervated, endplates are required for nodal sprouting (64).

These parallels suggest that neuron-intrinsic identity, injury-induced cues, and the structural and molecular context of the target together shape the capacity for adaptive circuit remodeling. Our *Drosophila* model provides a genetically tractable system to dissect these mechanisms with single-cell resolution and causal precision.

Conclusion and Perspective

Our study reveals that injury-induced heterosynaptic sprouting in the Drosophila motor circuit is triggered by complete loss of presynaptic input, is neuron-subtype specific, and contributes to functional recovery. These findings lay a foundation for uncovering the molecular logic of plasticity and circuit repair.

Drosophila offers a powerful model for dissecting the cellular and genetic mechanisms underlying this process. Future studies can use this system to identify the intrinsic growth

418 properties of specific neurons and the extrinsic cues that promote or restrict sprouting. These
419 insights may guide therapeutic strategies to enhance plasticity in motor disorders such as ALS
420 and spinal cord injury, and help test whether similar principles apply in vertebrate systems.
421
422
423

424 Materials and Methods

425

426 **Fly Husbandry**

427 All Crosses were reared at 25°C at 50% humidity with a 12 hr light/dark cycle. For crosses with
428 GTACR, larvae were fed with all-trans retinol (ATR) and kept in constant darkness until they
429 were ready to be imaged or dissected. Crosses involving RPR were at 29°C to ensure ablation
430 efficiency. For Larval ablation using Gal80ts, Embryos were kept at 25°C and as larvae hatched,
431 they transferred to 29°C to induce ablation. A list of stocks used can be found in Table S1.
432

433 **Fillet Dissection and Immunohistochemistry**

434 L3 larvae were used for fillet dissection, cutting on the ventral side. Dissections were fixed in 4%
435 PFA, blocked with equal parts 5% Goat serum and 5% Donkey serum in PBST, and stained with
436 primary and secondary antibodies. See SI Materials and methods and Table S2 for more details.
437

438 **NMJ Imaging and Quantification**

439 Airyscan Z-stacks were acquired using a Zeiss LSM900 Confocal with a 40x Objective and
440 processed with 3D Airyscan processing with the automatic filter. Postsynaptic Dlg of the neuron
441 of interest were isolated using a mask of the marked neuron and the area, bouton number and
442 bouton size were determined using a Fiji plugin developed by the Schneck lab. Branching points
443 were counted and separated based on colocalization with Dlg and the order of branching. See SI
444 Materials and Methods for more details.
445

446 **Behavioral Assays**

447 Larvae were placed in groves in a 2% agarose gel and recorded
448 (30 frames per second) using a smartphone mounted on a Zeiss Stemi 305 Microscope as they
449 crawled 1 cm. The number of peristalsis and frames for each peristalsis were counted to
450 determine the efficiency and duration, respectively. For analysis of overall crawling behavior,
451 Larvae were placed on a 2% agarose gel and recorded using a smartphone above the arena for 1

minute. The WrmTrck Plugin was utilized to determine the distance traveled and for each stage the ablatio group was normalized by the average of the control. See SI Materials and Methods for more details.

Intact Larvae Imaging and Muscle Calcium Imaging Quantification

Larvae were immobilized between a 2% agarose gel pad and a coverslip and imaged with 40x, 20x, or 10x, depending on the size of the larvae. Z-stacks of the marked axons at L0, L1, L2, and L3 were used to count the number of branching points. Time series of larvae undergoing peristalsis were analyzed using a custom MATLAB script to determine the intensity of the GCamp signal during peristalsis. See SI Materials and Methods for more details.

Statistical Analysis

All statistical analysis was performed using R in RStudio. Averages were plotted with SEM error bars and where applicable individual samples were added as points. Number of replicates and animals is indicated in figure legends. Kruskal Wallis and Dunn post hoc were used for all NMJ quantification and behavioral data, except the data in Figure 2 which used a t-test. To compare the L1 and L3 behavioral deficits, a t-test was used. Significance was established with * = $p<0.05$, ** = $p<0.01$, *** = $p<0.001$, ****=$p<0.0001$.

Acknowledgments

We are grateful to the Bloomington Drosophila Stock Center, Chris Doe, Troy Littleton, Dion Dickman, Keiko Hirono, Sarah Ackerman for generously providing transgenic fly lines. We also thank Lauren Carlisle and Elaina Hildner for their invaluable technical support. This research was funded by a grant from Texas A&M University.

References

1. N. Aderinto, M. O. AbdulBasit, G. Olatunji, T. Adejumo, Exploring the transformative influence of neuroplasticity on stroke rehabilitation: a narrative review of current evidence. *Ann Med Surg (Lond)* **85**, 4425-4432 (2023).
2. M. Bonanno, R. De Luca, A. M. De Nunzio, A. Quartarone, R. S. Calabro, Innovative Technologies in the Neurorehabilitation of Traumatic Brain Injury: A Systematic Review. *Brain Sci* **12** (2022).

3. C. T. Werner, C. J. Williams, M. R. Fermelia, D. T. Lin, Y. Li, Circuit Mechanisms of Neurodegenerative Diseases: A New Frontier With Miniature Fluorescence Microscopy. *Front Neurosci* **13**, 1174 (2019).
4. D. Tome, R. D. Almeida, Remaking a connection: molecular players involved in post-injury synapse formation. *Neural Regen Res* **20**, 1719-1720 (2025).
5. K. P. Menon, R. A. Carrillo, K. Zinn, Development and plasticity of the Drosophila larval neuromuscular junction. *Wiley interdisciplinary reviews. Developmental biology* **2**, 647-670 (2013).
6. Z. L. Newman *et al.*, Input-Specific Plasticity and Homeostasis at the Drosophila Larval Neuromuscular Junction. *Neuron* **93**, 1388-1404.e1310 (2017).
7. N. A. Aponte-Santiago, K. G. Ormerod, Y. Akbergenova, J. T. Littleton, Synaptic Plasticity Induced by Differential Manipulation of Tonic and Phasic Motoneurons in Drosophila. *The Journal of neuroscience : the official journal of the Society for Neuroscience* **40**, 6270-6288 (2020).
8. Y. Wang, M. Lobb-Rabe, J. Ashley, V. Anand, R. A. Carrillo, Structural and Functional Synaptic Plasticity Induced by Convergent Synapse Loss in the Drosophila Neuromuscular Circuit. *The Journal of neuroscience : the official journal of the Society for Neuroscience* **41**, 1401-1417 (2021).
9. C. C. Yifu Han, Pragya Goel, Kaikai He, Cristian Pinales, Chris Buser, Dion Dickman, Botulinum neurotoxin accurately separates tonic vs phasic transmission and reveals heterosynaptic plasticity rules in Drosophila. *bioRxiv* https://doi.org/10.1101/2022.02.15.480429 (2022).
10. Y. Wang *et al.*, Glial Draper signaling triggers cross-neuron plasticity in bystander neurons after neuronal cell death in Drosophila. *Nature communications* **14**, 4452 (2023).
11. Z. Lu *et al.*, High-Probability Neurotransmitter Release Sites Represent an Energy-Efficient Design. *Current biology : CB* **26**, 2562-2571 (2016).
12. G. A. Lnenicka, H. Keshishian, Identified motor terminals in Drosophila larvae show distinct differences in morphology and physiology. *Journal of neurobiology* **43**, 186-197 (2000).
13. N. A. Aponte-Santiago, J. T. Littleton, Synaptic Properties and Plasticity Mechanisms of Invertebrate Tonic and Phasic Neurons. *Front Physiol* **11**, 611982 (2020).
14. R. P. Dum, T. T. Kennedy, Physiological and histochemical characteristics of motor units in cat tibialis anterior and extensor digitorum longus muscles. *Journal of neurophysiology* **43**, 1615-1630 (1980).
15. S. W. Kuffler, E. M. Vaughan Williams, Properties of the 'slow' skeletal muscles fibres of the frog. *The Journal of physiology* **121**, 318-340 (1953).
16. H. Atwood, Parallel 'phasic' and 'tonic' motor systems of the crayfish abdomen. *The Journal of experimental biology* **211**, 2193-2195 (2008).
17. C. A. Frank *et al.*, New approaches for studying synaptic development, function, and plasticity using Drosophila as a model system. *The Journal of neuroscience : the official journal of the Society for Neuroscience* **33**, 17560-17568 (2013).
18. G. W. Davis, M. Müller, Homeostatic control of presynaptic neurotransmitter release. *Annu Rev Physiol* **77**, 251-270 (2015).
19. K. P. Harris, J. T. Littleton, Transmission, Development, and Plasticity of Synapses. *Genetics* **201**, 345-375 (2015).
20. O. Genc, G. W. Davis, Target-wide Induction and Synapse Type-Specific Robustness of Presynaptic Homeostasis. *Current biology : CB* **29**, 3863-3873 e3862 (2019).

536 21. P. Goel *et al.*, Homeostatic scaling of active zone scaffolds maintains global synaptic
537 strength. *Journal of Cell Biology* **218**, 1706-1724 (2019).
538 22. T. D. James, D. J. Zwiefelhofer, C. A. Frank, Maintenance of homeostatic plasticity at the
539 Drosophila neuromuscular synapse requires continuous IP(3)-directed signaling. *eLife* **8**
540 (2019).
541 23. C. A. Frank, T. D. James, M. Müller, Homeostatic control of Drosophila neuromuscular
542 junction function. *Synapse* **74**, e22133 (2020).
543 24. X. Li *et al.*, Autocrine inhibition by a glutamate-gated chloride channel mediates
544 presynaptic homeostatic depression. *Science Advances* **7**, eabj1215 (2021).
545 25. C. J. Yeates, C. A. Frank, Homeostatic Depression Shows Heightened Sensitivity to
546 Synaptic Calcium. *Front Cell Neurosci* **15**, 618393 (2021).
547 26. N. S. Armstrong, C. A. Frank, The calcineurin regulator Sarah enables distinct forms of
548 homeostatic plasticity at the Drosophila neuromuscular junction. *Front Synaptic*
549 *Neurosci* **14**, 1033743 (2022).
550 27. Y. Han *et al.*, Botulinum neurotoxin accurately separates tonic vs. phasic transmission
551 and reveals heterosynaptic plasticity rules in Drosophila. *eLife* **11**, e77924 (2022).
552 28. K. He *et al.*, Physiologic and Nanoscale Distinctions Define Glutamatergic Synapses in
553 Tonic vs Phasic Neurons. *The Journal of neuroscience : the official journal of the Society*
554 *for Neuroscience* **43**, 4598-4611 (2023).
555 29. T. Wang, C. A. Frank, Using Electrophysiology to Study Homeostatic Plasticity at the
556 Drosophila Neuromuscular Junction. *Cold Spring Harb Protoc* 10.1101/pdb.top108393
557 (2024).
558 30. M. Landgraf, T. Bossing, G. M. Technau, M. Bate, The origin, location, and projections of
559 the embryonic abdominal motorneurons of Drosophila. *The Journal of neuroscience : the*
560 *official journal of the Society for Neuroscience* **17**, 9642-9655 (1997).
561 31. B. Hoang, A. Chiba, Single-cell analysis of Drosophila larval neuromuscular synapses.
562 *Developmental biology* **229**, 55-70 (2001).
563 32. M. Landgraf, V. Jeffrey, M. Fujioka, J. B. Jaynes, M. Bate, Embryonic origins of a motor
564 system: motor dendrites form a myotopic map in Drosophila. *PLoS biology* **1**, E41 (2003).
565 33. M. Landgraf, S. Thor, Development of Drosophila motoneurons: specification and
566 morphology. *Seminars in cell & developmental biology* **17**, 3-11 (2006).
567 34. M. F. Zwart *et al.*, Selective Inhibition Mediates the Sequential Recruitment of Motor
568 Pools. *Neuron* **91**, 615-628 (2016).
569 35. A. A. Zarin, J. P. Labrador, Motor axon guidance in Drosophila. *Seminars in cell &*
570 *developmental biology* 10.1016/j.semcdb.2017.11.013 (2017).
571 36. A. A. Zarin, B. Mark, A. Cardona, A. Litwin-Kumar, C. Q. Doe, A multilayer circuit
572 architecture for the generation of distinct locomotor behaviors in Drosophila. *eLife* **8**
573 (2019).
574 37. P. C. Cooney *et al.*, Neuromuscular basis of Drosophila larval rolling escape behavior.
575 *Proceedings of the National Academy of Sciences of the United States of America* **120**,
576 e2303641120 (2023).
577 38. S. K. Jetti *et al.*, Molecular logic of synaptic diversity between Drosophila tonic and
578 phasic motoneurons. *Neuron* **111**, 3554-3569 e3557 (2023).
579 39. L. Goyal, K. McCall, J. Agapite, E. Hartwieg, H. Steller, Induction of apoptosis by
580 Drosophila reaper, hid and grim through inhibition of IAP function. *The EMBO journal*
581 **19**, 589-597 (2000).
582 40. J. J. Perez-Moreno, C. J. O'Kane, GAL4 Drivers Specific for Type Ib and Type Is Motor
583 Neurons in Drosophila. *G3 (Bethesda, Md.)* **9**, 453-462 (2019).

584 41. B. Nijhof *et al.*, A New Fiji-Based Algorithm That Systematically Quantifies Nine Synaptic
585 Parameters Provides Insights into Drosophila NMJ Morphometry. *PLoS computational*
586 *biology* **12**, e1004823 (2016).
587 42. A. Castells-Nobau *et al.*, Two Algorithms for High-throughput and Multi-parametric
588 Quantification of Drosophila Neuromuscular Junction Morphology. *J Vis Exp*
589 10.3791/55395 (2017).
590 43. S. E. McGuire, P. T. Le, A. J. Osborn, K. Matsumoto, R. L. Davis, Spatiotemporal rescue of
591 memory dysfunction in Drosophila. *Science (New York, N.Y.)* **302**, 1765-1768 (2003).
592 44. M. L. Suster, L. Seugnet, M. Bate, M. B. Sokolowski, Refining GAL4-driven transgene
593 expression in Drosophila with a GAL80 enhancer-trap. *Genesis* **39**, 240-245 (2004).
594 45. A. Carreira-Rosario *et al.*, MDN brain descending neurons coordinately activate
595 backward and inhibit forward locomotion. *eLife* **7** (2018).
596 46. A. S. Mauss, C. Busch, A. Borst, Optogenetic Neuronal Silencing in Drosophila during
597 Visual Processing. *Scientific reports* **7**, 13823 (2017).
598 47. F. Mohammad *et al.*, Optogenetic inhibition of behavior with anion channelrhodopsins.
599 *Nature methods* **14**, 271-274 (2017).
600 48. A. Sitaula, Y. Huang, A. Zarin, Application of a Dual Optogenetic Silencing-Activation
601 Protocol to Map Motor Neurons Driving Rolling Escape Behavior in Drosophila Larvae.
602 *Bio Protoc* **14**, e5131 (2024).
603 49. A. A. Z. Yuhan Huang, A premotor microcircuit to generate behavior-specific muscle
604 activation patterns in Drosophila larvae. *bioRxiv*
605 https://doi.org/10.1101/2022.08.18.504452 (2022).
606 50. S. T. Sweeney, K. Broadie, J. Keane, H. Niemann, C. J. O'Kane, Targeted expression of
607 tetanus toxin light chain in Drosophila specifically eliminates synaptic transmission and
608 causes behavioral defects. *Neuron* **14**, 341-351 (1995).
609 51. T. N. Chang, H. Keshishian, Laser ablation of Drosophila embryonic motoneurons causes
610 ectopic innervation of target muscle fibers. *The Journal of neuroscience : the official*
611 *journal of the Society for Neuroscience* **16**, 5715-5726 (1996).
612 52. S. D. Ackerman, N. A. Perez-Catalan, M. R. Freeman, C. Q. Doe, Astrocytes close a motor
613 circuit critical period. *Nature* **592**, 414-420 (2021).
614 53. T. H. Nguyen *et al.*, scRNA-seq data from the larval Drosophila ventral cord provides a
615 resource for studying motor systems function and development. *Dev Cell* **59**, 1210-1230
616 e1219 (2024).
617 54. A. T. Medeiros, S. J. Gratz, A. Delgado, J. T. Ritt, K. M. O'Connor-Giles, Ca(2+) channel
618 and active zone protein abundance intersects with input-specific synapse organization
619 to shape functional synaptic diversity. *eLife* **12** (2024).
620 55. T. Hagg, Collateral sprouting as a target for improved function after spinal cord injury. *J*
621 *Neurotrauma* **23**, 281-294 (2006).
622 56. N. Weidner, A. Ner, N. Salimi, M. H. Tuszynski, Spontaneous corticospinal axonal
623 plasticity and functional recovery after adult central nervous system injury. *Proceedings*
624 *of the National Academy of Sciences of the United States of America* **98**, 3513-3518
625 (2001).
626 57. Y. Nakamura *et al.*, Modulation of Both Intrinsic and Extrinsic Factors Additively
627 Promotes Rewiring of Corticospinal Circuits after Spinal Cord Injury. *The Journal of*
628 *neuroscience : the official journal of the Society for Neuroscience* **41**, 10247-10260
629 (2021).

630 58. S. F. Kazim *et al.*, Corticospinal Motor Circuit Plasticity After Spinal Cord Injury:
631 Harnessing Neuroplasticity to Improve Functional Outcomes. *Mol Neurobiol* **58**, 5494-
632 5516 (2021).
633 59. M. Chen, B. Zheng, Axon plasticity in the mammalian central nervous system after
634 injury. *Trends Neurosci* **37**, 583-593 (2014).
635 60. J. P. Kapfhammer, Axon sprouting in the spinal cord: growth promoting and growth
636 inhibitory mechanisms. *Anat Embryol (Berl)* **196**, 417-426 (1997).
637 61. S. Bolivar, X. Navarro, E. Udina, Schwann Cell Role in Selectivity of Nerve Regeneration.
638 *Cells* **9** (2020).
639 62. I. C. Maier, M. E. Schwab, Sprouting, regeneration and circuit formation in the injured
640 spinal cord: factors and activity. *Philosophical transactions of the Royal Society of*
641 *London. Series B, Biological sciences* **361**, 1611-1634 (2006).
642 63. M. C. Brown, R. L. Holland, A central role for denervated tissues in causing nerve
643 sprouting. *Nature* **282**, 724-726 (1979).
644 64. R. J. Keynes, W. G. Hopkins, M. C. Brown, Sprouting of mammalian motor neurones at
645 nodes of Ranvier: the role of the denervated motor endplate. *Brain research* **264**, 209-
646 213 (1983).

647

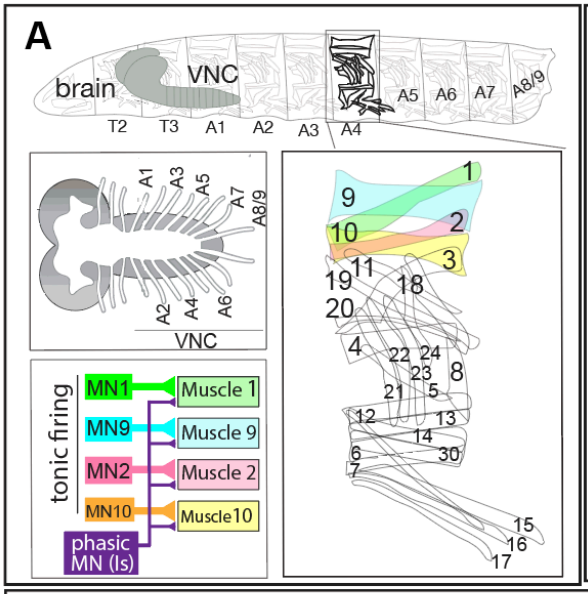
A
brain
VNC
T2
T3
A1
A2
A3
A4
A5
A6
A7
A8/9
VNC
tonic firing
MN1
MN9
MN2
MN10
phasic MN (Is)
Muscle 1
Muscle 9
Muscle 2
Muscle10

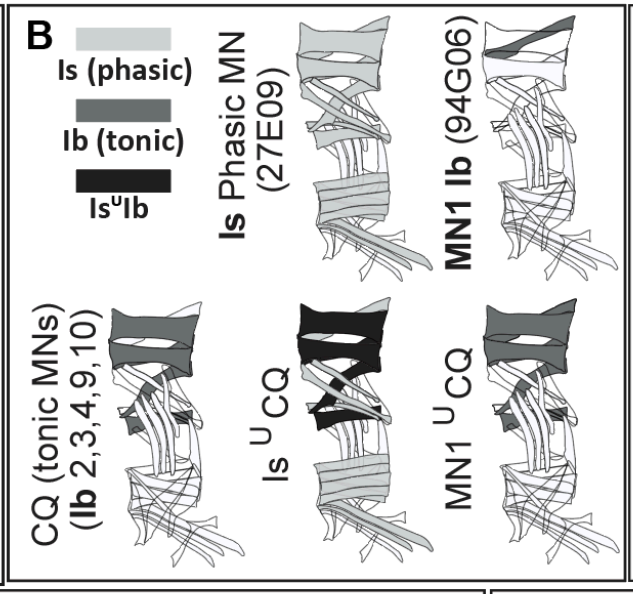
B
Is (phasic)
Ib (tonic)
IsᵘIb
Is Phasic MN (27E09)
MN1 Ib (94G06)
CQ (tonic MNs) (Ib 2,3,4,9,10)
Is ᵘCQ
MN1 ᵘCQ

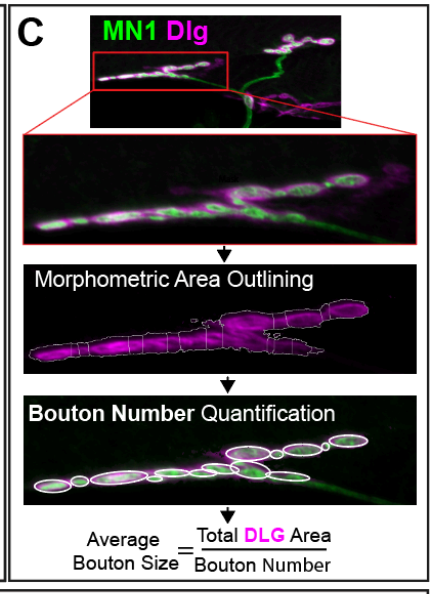
C
MN1 Dlg
Morphometric Area Outlining
Bouton Number Quantification
Average Bouton Size = Total DLG Area / Bouton Number

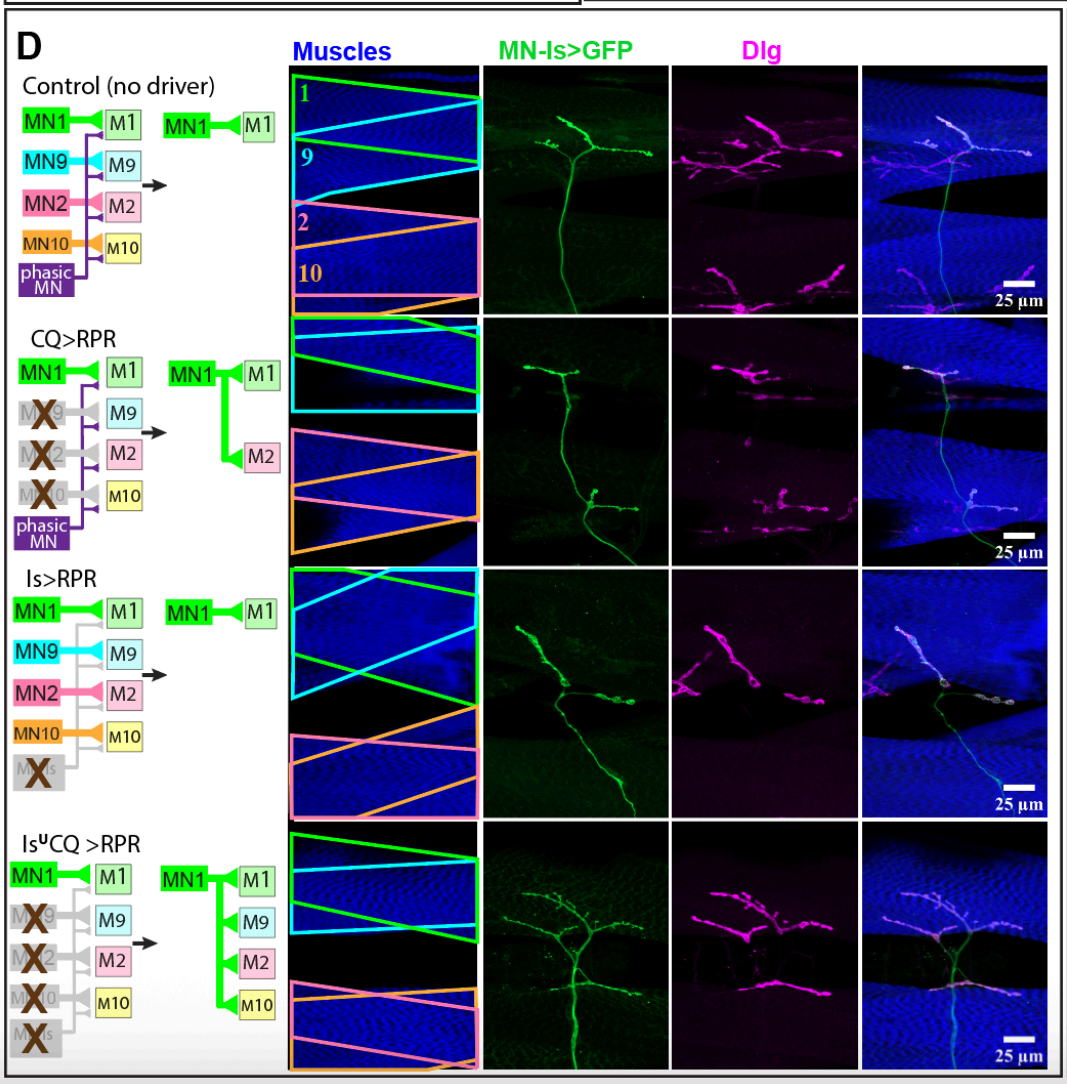
D
Muscles
MN-Is>GFP
Dlg
Control (no driver)
CQ>RPR
Is>RPR
IsᵘCQ >RPR
MN1
MN9
MN2
MN10
phasic MN
M1
M9
M2
M10
25 µm

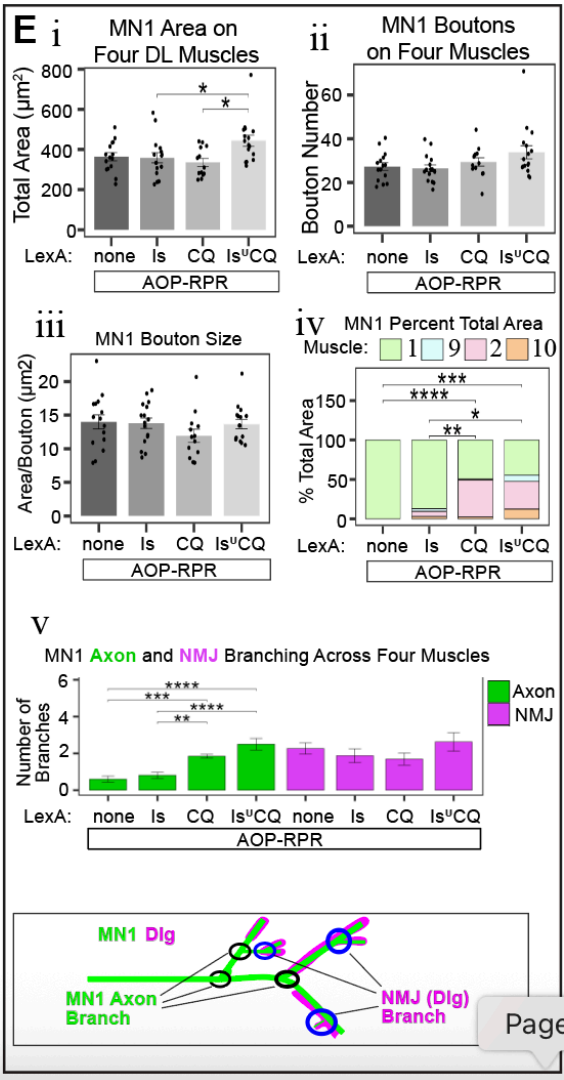
E
i
MN1 Area on Four DL Muscles
Total Area (µm²)
ii
MN1 Boutons on Four Muscles
Bouton Number
iii
MN1 Bouton Size
Area/Bouton (µm2)
iv
MN1 Percent Total Area
Muscle: 1 9 2 10
% Total Area
LexA: none Is CQ IsᵘCQ
AOP-RPR
v
MN1 Axon and NMJ Branching Across Four Muscles
Number of Branches
Axon
NMJ
MN1 Dlg
MN1 Axon Branch
NMJ (Dlg) Branch

659
660
661
662

663 **Figure 1. The tonic MN1 axon sprouts and forms ectopic NMJs on fully denervated**
664 **dorsal-longitudinal (DL) muscles.**
665 (A) Schematic diagrams of the Drosophila larval nervous system and body wall muscles.
666 This study focuses on four DL muscles (1, 2, 9, and 10), each receiving phasic input from
667 a common phasic MN-Is and tonic input from distinct tonic Ib MNs (MN1, MN2, MN9,
668 and MN10).
669 (B) Target muscles of the Gal4 and LexA MN drivers used in this study. The union
670 symbol (∪) indicates fly lines carrying two drivers simultaneously. For example, in *Is ∪*
671 *CQ* larvae, both tonic and phasic MNs innervating muscles 2, 3, 4, 9, and 10 are targeted.
672 (C) Workflow illustrating the NMJ analysis pipeline [adapted from (41, 42)].
673 (D) Representative NMJ immunostaining visualizing the bystander MN1 axon in
674 different genotypes: control, phasic MN-Is ablated (*Is>RPR*), tonic MN2, MN9, MN10
675 ablated (*CQ>RPR*), and both tonic and phasic MNs ablated (*Is ∪ CQ>RPR*). Schematics
676 (left) depict ablated MNs and their effects on MN1. In controls, MN1 exclusively
677 innervates muscle 1 (top row), and this pattern is unchanged after phasic MN-Is ablation
678 (second row). Ablation of tonic MNs (CQ>RPR) induces sprouting of MN1 onto muscle
679 2 (M2). Co-ablation of tonic and phasic MNs (*Is ∪ CQ>RPR*) induces robust MN1
680 sprouting, forming ectopic NMJs on all nearby denervated muscles (M2, M9, M10) in
681 addition to its native target (M1). Postsynaptic sites are marked by Dlg (magenta) and
682 muscles by phalloidin (blue). MN1 is labeled with UAS-myr-GFP driven by 94G06-
683 Gal4; targeted MN ablation is achieved using the LexA/OP-RPR system.
684 (E) Quantification of MN1 axon and NMJ parameters across groups shown in (D).
685 (i) Total MN1 area on DL muscles 1, 2, 9, and 10. *Is ∪ CQ>RPR* larvae exhibit
686 significantly increased total MN1 surface area relative to control and other ablation
687 groups.
688 (ii) Total number of MN1 boutons on DL muscles. No significant differences across
689 groups.

690 (iii) Average bouton size (area/bouton number). No significant differences across groups.
691 (iv) Proportional distribution of MN1 NMJ area on individual DL muscles. In CQ>RPR
692 larvae, MN1 ectopically innervates muscle 2; in *Is ∪ CQ>RPR* larvae, MN1 innervates
693 muscles 2, 9, and 10 in addition to its native target Muscle 1. The area on Muscle 1 is
694 significantly decreased compared to control group.
695
696 (v) Average number of motor axon branching points (green) and NMJ branching points.
697 *CQ>RPR* and *Is ∪CQ>RPR* groups exhibit significantly increased axon branching
698 compared to control group.

699 For control, *Is>RPR*, and *Is ∪ CQ>RPR*, n = 8 larvae (16 hemisegments). For *CQ>RPR*,
700 n = 7 larvae (13 hemisegments). Data points represent single hemisegments. Error bars:
701 ±SEM. Statistical analysis: Kruskal-Wallis with Dunn's post-hoc test (*p<0.05;
702 **p<0.01; ***p<0.001; ****p<0.0001*).

703
704
705
706
707
708
709
710
711
712
713

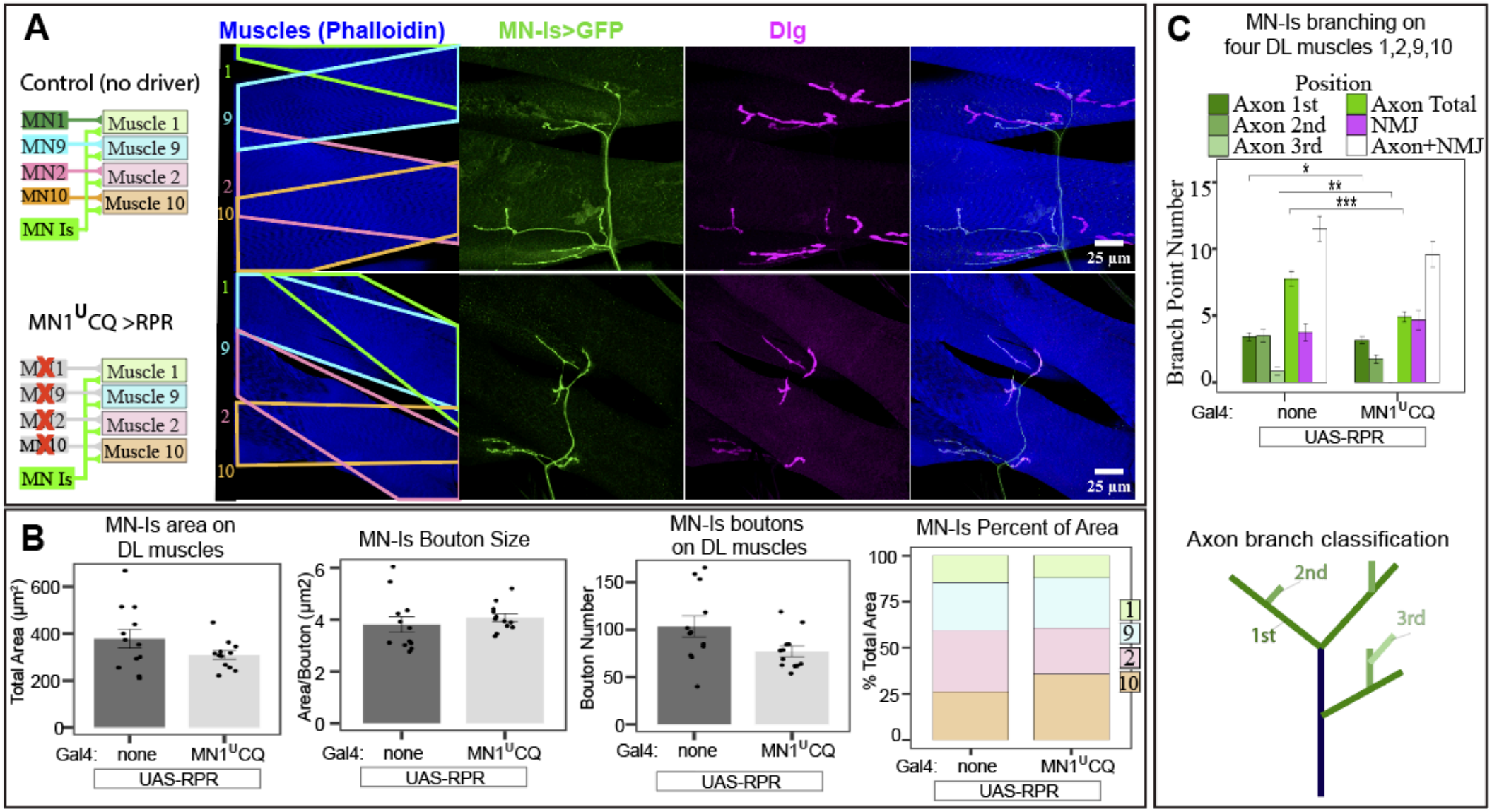
A
Muscles (Phalloidin)
MN-Is>GFP
Dlg
Control (no driver)
MN1
MN9
MN2
MN10
MN Is
Muscle 1
Muscle 9
Muscle 2
Muscle 10
MN1UCQ >RPR
25 µm
B
MN-Is area on DL muscles
Total Area (µm²)
MN-Is Bouton Size
Area/Bouton (µm2)
MN-Is boutons on DL muscles
Bouton Number
MN-Is Percent of Area
% Total Area
Gal4: none MN1UCQ
UAS-RPR
C
MN-Is branching on four DL muscles 1,2,9,10
Position
Axon 1st
Axon 2nd
Axon 3rd
Axon Total
NMJ
Axon+NMJ
Branch Point Number
Axon branch classification
1st
2nd
3rd

736
737
738
739
740

741 **Figure 2. Phasic MN-Is does not exhibit structural expansion following ablation of**
742 **tonic MNs innervating dorsal-longitudinal (DL) muscles.**
743 (A) Representative NMJ immunostaining showing the bystander phasic MN-Is axon in
744 control larvae and in larvae where all tonic Ib MNs innervating DL muscles (MN1, MN2,
745 MN9, MN10) were ablated (*MN1 ∪ CQ>RPR*). Postsynaptic sites are labeled with Dlg
746 (magenta), muscles with phalloidin (blue), and MN-Is axons with myr-GFP driven by the
747 27E09 enhancer. Ablation of tonic MNs was achieved using the 94G06-Gal4 ∪ CQ-Gal4
748 / UAS-RPR system.
749 (B) Quantification of Is NMJ parameters shows no significant differences in total NMJ
750 area, bouton size, bouton number, or NMJ area distribution between control and *MN1 ∪*
751 *CQ>RPR* larvae. Each data point represents a single hemisegment.
752 (C) Ablation of tonic MNs results in a significant reduction in 2nd- and 3rd-order axonal
753 branches of the bystander MN-Is.

754 For both control and *MN1 ∪ CQ>RPR* groups, n = 6 larvae (12 hemisegments). Data
755 points represent individual hemisegments. Error bars indicate mean ± SEM. Statistical
756 analysis: Kruskal-Wallis with Dunn's post-hoc test ($p<0.05$; *$p<0.01$; **$p<0.001$;
757 ***$p<0.0001$).

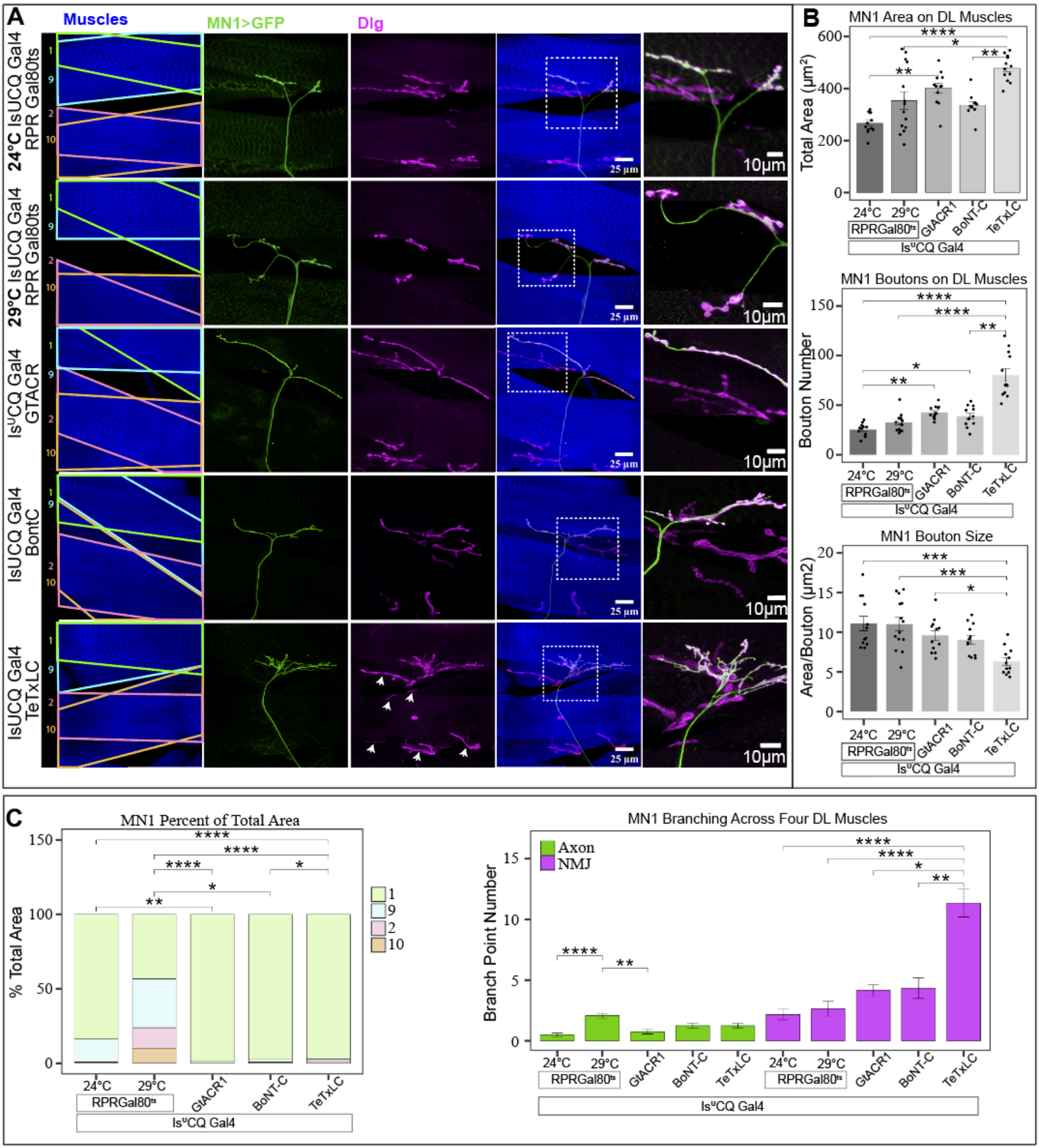
A
Muscles
MN1>GFP
Dlg
24°C IsUCQ Gal4 RPR Gal80ts
29°C IsUCQ Gal4 RPR Gal80ts
IsUCQ Gal4 GTACR
IsUCQ Gal4 BontC
IsUCQ Gal4 TeTxLC
1
9
2
10
25 µm
10µm
B
MN1 Area on DL Muscles
Total Area (µm²)
MN1 Boutons on DL Muscles
Bouton Number
MN1 Bouton Size
Area/Bouton (µm2)
24°C
29°C
RPRGal80ts
GtACR1
BoNT-C
TeTxLC
IsUCQ Gal4
C
MN1 Percent of Total Area
% Total Area
MN1 Branching Across Four DL Muscles
Branch Point Number
Axon
NMJ

769
770

771 **Figure 3. The bystander MN1 exhibits distinct structural responses to different**
772 **perturbations of neighboring MNs.**
773 (A–C) Representative images (A) and quantitative analyses (B–C) of MN1 axons and
774 NMJs across genotypes. MN1 is labeled with MN1-lexA >AOP-myr-GFP.

775 In control animals (CQ ∪ Is-Gal4/UAS-RPR, Gal80^{ts} raised at 24°C), MN1 shows normal
776 axon and NMJ morphology. In the ablation group (CQ ∪ Is-Gal4/UAS-RPR, Gal80^{ts}
777 raised at 29°C), MN1 exhibits robust sprouting, forming ectopic NMJs on denervated
778 muscles 2, 9, and 10.

779 In the acute silencing group (CQ ∪ Is-Gal4/UAS-GtACR1), MN1 NMJ area and bouton
780 number are elevated relative to controls, but no ectopic sprouting onto muscles 2, 9, and
781 10 is observed.

782 In the chronic silencing group targeting both evoked and spontaneous release (CQ ∪ Is-
783 Gal4/UAS-BoNT-C), MN1 shows increased bouton numbers without ectopic sprouting.

784 In the chronic silencing group targeting only evoked release (CQ ∪ Is-Gal4/UAS-
785 TeTxLC), MN1 NMJ branching, area, and bouton number are markedly increased
786 compared to controls and other perturbations. However, bouton size is significantly
787 reduced, and no ectopic sprouting onto muscles 2, 9, and 10 occurs. Notably, the overall
788 NMJ morphology of TeTxLC-silenced tonic and phasic MNs (white arrows) appears
789 normal based on Dlg staining.

790 Data points represent single hemisegments. Ablation group: n=7 larvae (14
791 hemisegments). All other groups: n=6 larvae (12 hemisegments). Error bars: ±SEM.
792 Kruskal-Wallis with Dunn's post-hoc test (*$p<0.05$; **$p<0.01$; ***$p<0.001$;
793 ****$p<0.0001$).

794

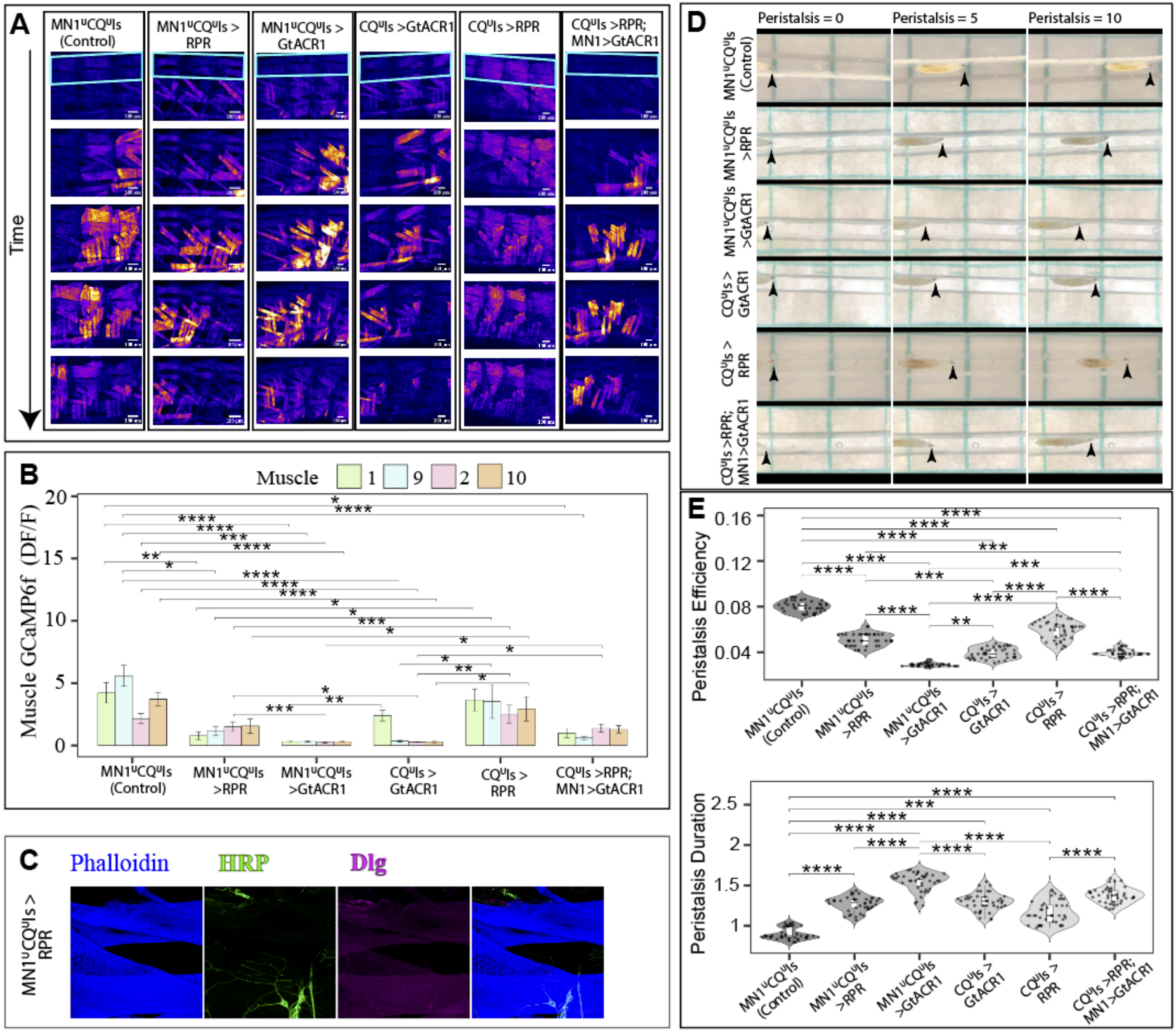
A
MN1ᵘCQᵘIs (Control)
MN1ᵘCQᵘIs > RPR
MN1ᵘCQᵘIs > GtACR1
CQᵘIs >GtACR1
CQᵘIs >RPR
CQᵘIs >RPR; MN1>GtACR1
Time
B
Muscle 1 9 2 10
Muscle GCaMP6f (DF/F)
MN1ᵘCQᵘIs (Control)
MN1ᵘCQᵘIs >RPR
MN1ᵘCQᵘIs >GtACR1
CQᵘIs > GtACR1
CQᵘIs > RPR
CQᵘIs >RPR; MN1>GtACR1
C
Phalloidin
HRP
Dlg
MN1ᵘCQᵘIs > RPR
D
Peristalsis = 0
Peristalsis = 5
Peristalsis = 10
E
Peristalsis Efficiency
Peristalsis Duration

812 **Figure 4. Ectopic NMJs formed by sprouting MN1 are functional and improve**
813 **larval locomotion.**
814 (A) Muscle calcium imaging in intact, forward-crawling larvae of different genotypes.
815 Each column shows still images from three adjacent abdominal segments at successive
816 time points during a forward peristaltic wave. GCaMP6f fluorescence (expressed under
817 the 44H10 muscle-specific enhancer) increases during muscle contraction. Cyan
818 rectangles mark dorsal-longitudinal (DL) muscles in the top panels. In control larvae
819 (MN1 ∪ CQ ∪ Is-lexA/ Aop-GTACR ATR (-)), DL muscles contract sequentially, with
820 GCaMP6f signals propagating from posterior (right) to anterior (left) during crawling.
821 Ablation of all tonic and phasic MNs (MN1 ∪ CQ ∪ Is-lexA/Aop-RPR) abolishes DL
822 muscle activity, leaving ventral and lateral muscles unaffected. Similarly, acute silencing
823 of these MNs (MN1 ∪ CQ ∪ Is-lexA/Aop-GtACR1 ATR (+)) eliminates DL muscle
824 activity. In CQ ∪ Is-lexA/Aop-GtACR1 ATR (+) larvae, only Muscle 1 remains active,
825 consistent with preserved MN1 input. In contrast, CQ ∪ Is-lexA/Aop-RPR larvae exhibit
826 robust calcium activity and contractions in all four DL muscles, indicating functional
827 reinnervation by sprouted MN1. Acute silencing of the sprouted MN1 in CQ ∪ Is-
828 lexA/Aop-RPR; MN1-Gal4>UAS-GtACR1 ATR (+) larvae abolishes DL muscle
829 activity. Frames are taken from Supplementary Video X.

830 (B) Quantification of GCaMP6f signal in DL muscles (1, 2, 9, and 10) confirms
831 observations in (A). n = 5 larvae per genotype (10 hemisegments total). Statistical
832 analysis: Kruskal–Wallis test with Dunn's post-hoc correction (*$p<0.05$, **$p<0.01$,
833 ***$p<0.001$, ****$p<0.0001$).

834 (C) Immunostaining of DL muscles in MN1 ∪ CQ ∪ Is-lexA/Aop-RPR larvae verifies
835 complete ablation of targeted MNs. Anti-HRP (green) labels the nearby sensory neurons,
836 and no motor axons or Dlg puncta are detected in denervated DL muscles.

837 (D) Representative crawling trajectories of larvae from the genotypes in (A). Each row
838 shows larval positions at the start line (Peristalsis = 0), after 5 peristalses, and after 10
839 peristalses. Among all groups, control larvae (MN1 ∪ CQ ∪ Is-lexA/+) ranked first in
840 distance traveled, followed by CQ ∪ Is-lexA/Aop-RPR larvae, which ranked second. In

841 contrast, MN1 ∪ CQ ∪ Is-lexA/Aop-GtACR1 larvae showed the least forward
842 progression.

843 (E) Quantification of peristalsis efficiency (distance traveled per peristaltic wave) and
844 peristalsis duration (time required to complete a wave). Control larvae (MN1 ∪ CQ ∪ Is-
845 lexA/+) exhibited the highest peristalsis efficiency and shortest duration, followed by CQ
846 ∪ Is-lexA/Aop-RPR larvae. Silencing the sprouted MN1 in CQ ∪ Is-lexA/Aop-RPR;
847 MN1-Gal4>UAS-GtACR1 larvae reduced locomotor performance to levels comparable
848 with other two silenced groups. n = 40 larvae per group, with each dot representing an
849 individual animal. Statistical analysis: One-way ANOVA with Tukey post-hoc test
850 (*$p<0.05$, **$p<0.01$, ***$p<0.001$, ****$p<0.0001$).

851
852
853

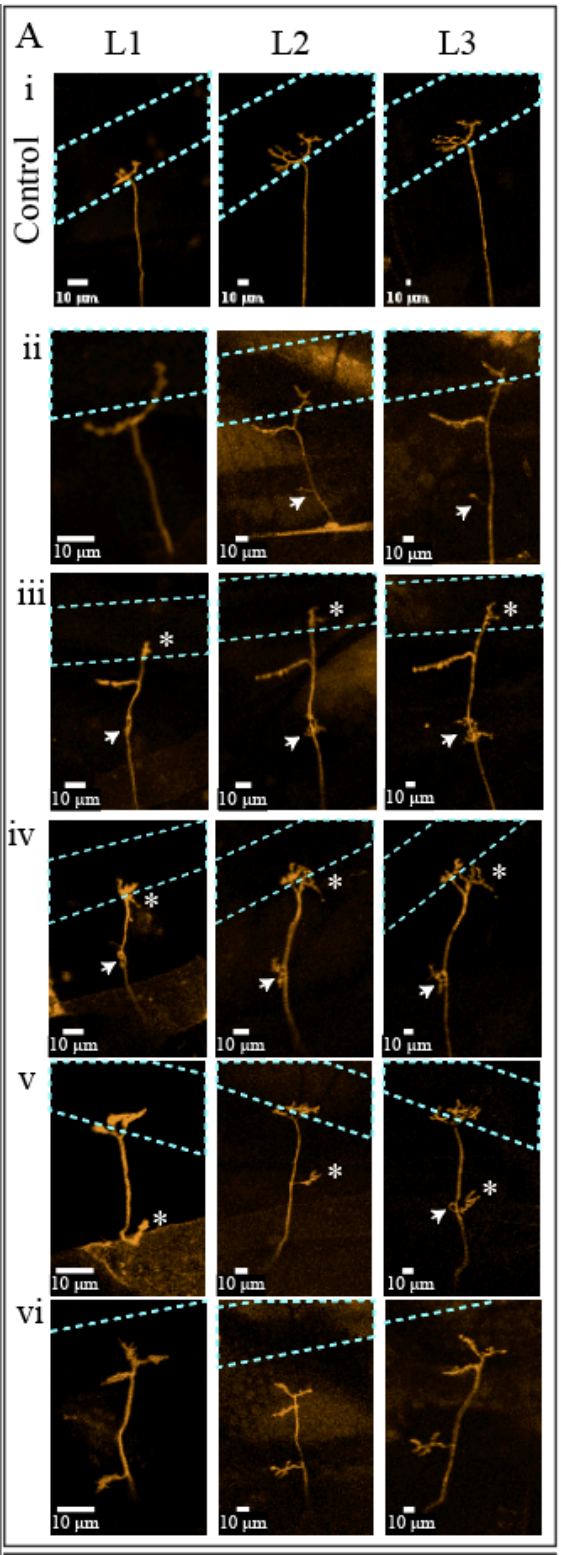
A
L1
L2
L3
i
Control
ii
iii
iv
v
vi
10 µm

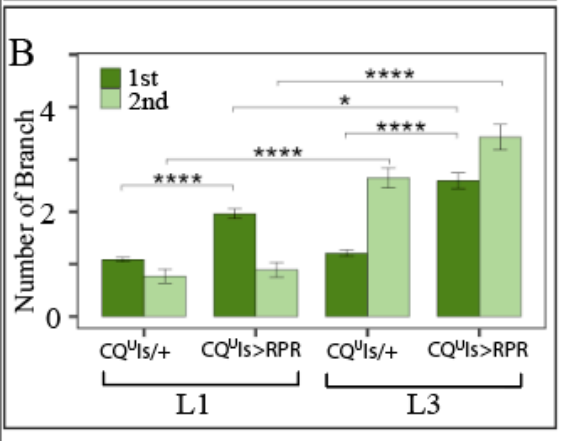
B
1st
2nd
Number of Branch
0
2
4
****
*
CQUIs/+
CQUIs>RPR
L1
L3

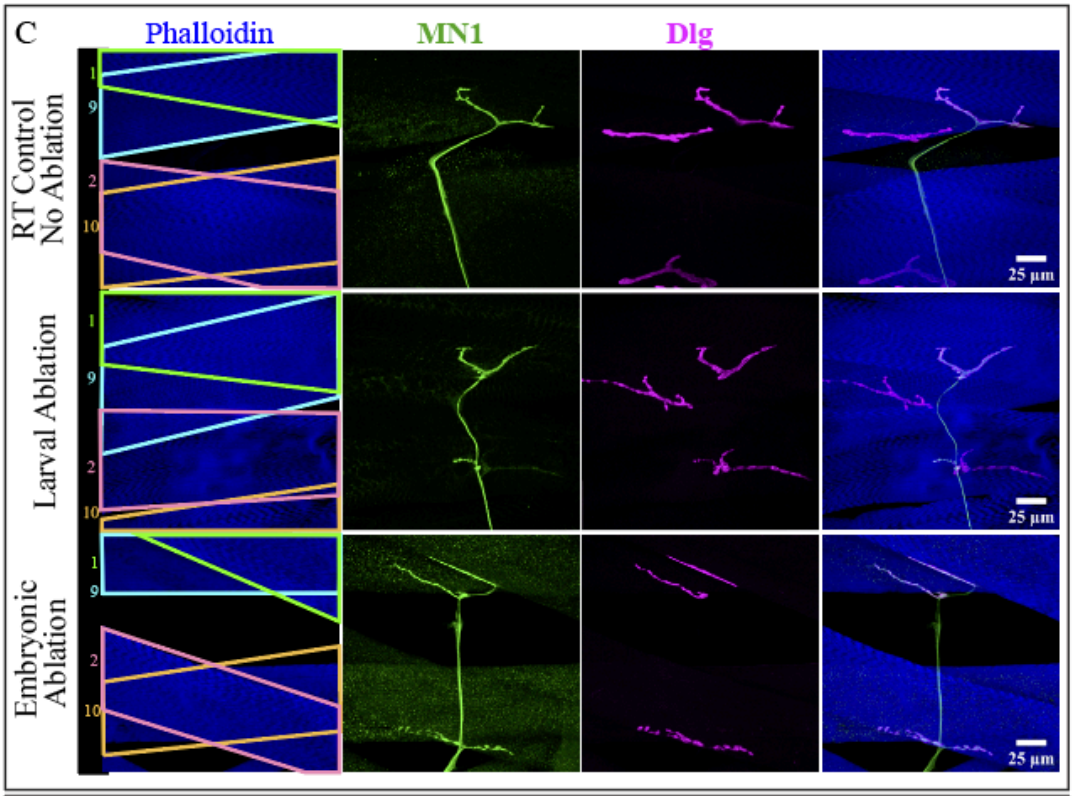
C
Phalloidin
MN1
Dlg
RT Control No Ablation
Larval Ablation
Embryonic Ablation
1
9
2
10
25 µm

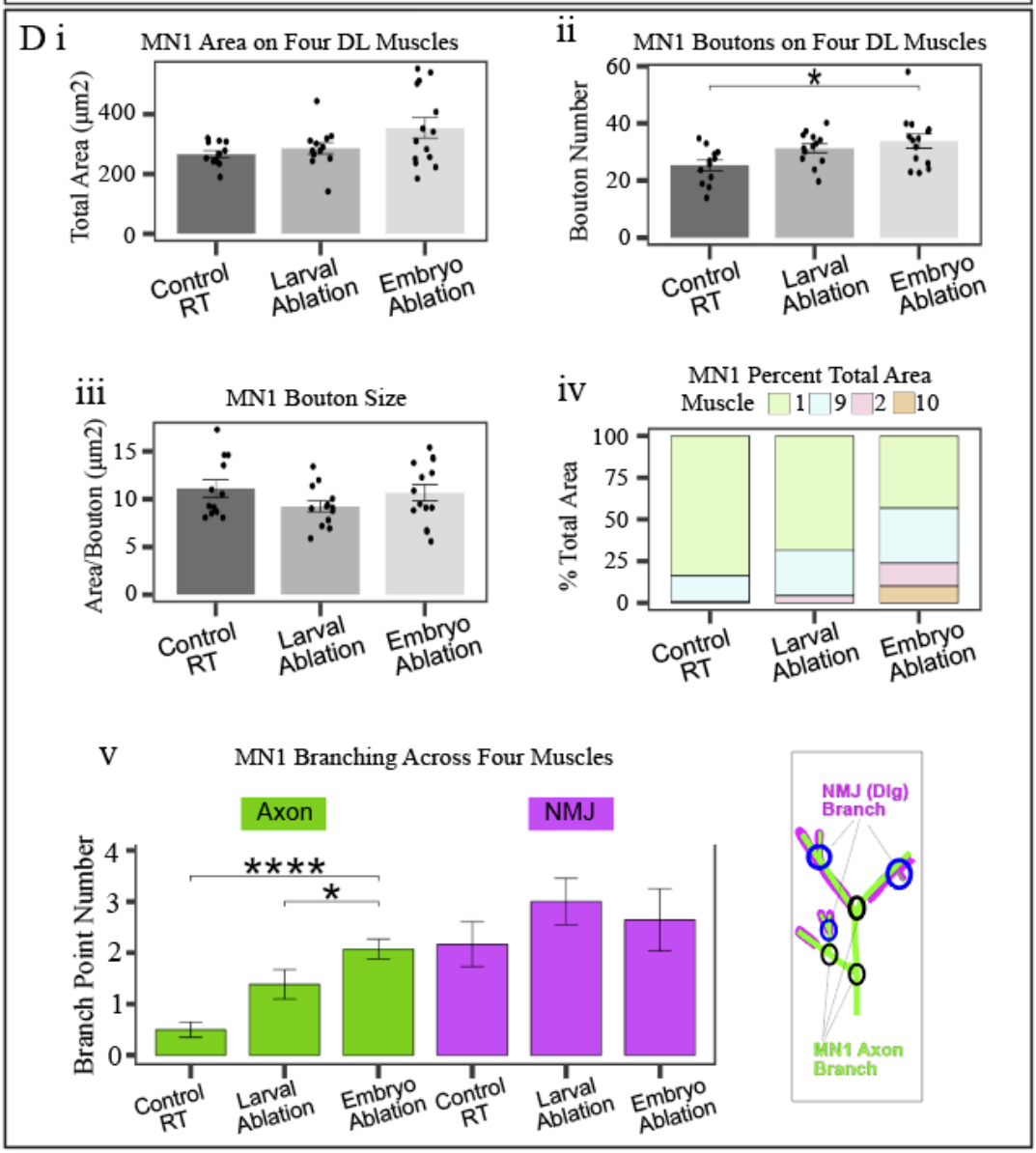
D i
MN1 Area on Four DL Muscles
Total Area (µm2)
0
200
400
Control RT
Larval Ablation
Embryo Ablation
ii
MN1 Boutons on Four DL Muscles
Bouton Number
0
20
40
60
*
iii
MN1 Bouton Size
Area/Bouton (µm2)
0
5
10
15
iv
MN1 Percent Total Area
Muscle 1 9 2 10
% Total Area
0
25
50
75
100
v
MN1 Branching Across Four Muscles
Axon
NMJ
Branch Point Number
0
1
2
3
4
****
*
Control RT
Larval Ablation
Embryo Ablation
NMJ (Dlg) Branch
MN1 Axon Branch

862
863

864 **Figure 5. MN1 axon sprouting dynamics and timing of injury-induced plasticity**
865 (A) Live imaging of MN1 axons across larval stages. Each row shows stills from the
866 same hemisegment at L1, L2, and L3.
867 (i) In a control larva (CQ ∪ Is-Gal4/+; MN1-lexA >Aop-tdTomato), MN1 innervates its
868 native target muscle 1 (cyan box) by L1. The axon terminal arborizes further between
869 L1–L3, with the main shaft bifurcating beneath muscle 1 to form a T-shaped NMJ.
870 (ii–vi) In ablated larvae (CQ ∪ Is-Gal4/UAS-RPR; MN1-lexA >Aop-tdTomato), diverse
871 sprouting patterns are observed:
872 (ii) New axon branches (white arrow) emerge at L2 and grow further by L3.
873 (iii–v) Small axon buds appear at L1 (white arrows) and expand progressively in L2 and
874 L3. Some branches (white asterisks) are already present at L1 and undergo marked
875 growth during later stages.
876 (vi) In rare cases, MN1 fails to reach its native target muscle 1 and instead branches
877 prematurely to innervate other DL muscles.

878 (B) Quantification of 1st- and 2nd-order axon branches in L1 and L3 stages for controls
879 and ablated animals. At L1, ablated larvae show ~2× more 1st-order branches than
880 controls, with comparable 2nd-order branching. By L3, ablated larvae exhibit
881 significantly more 1st-order branches than controls. Within ablated larvae, both branch
882 types increase markedly from L1 to L3; in controls, only 2nd-order branching increases
883 over time. Data points represent single hemisegments (L1 control: n=5 larvae, 57
884 hemisegments; L1 ablation: n=5 larvae, 56 hemisegments; L3 control: n=5 larvae, 57
885 hemisegments; L3 ablation: n=5 larvae, 54 hemisegments). Error bars: ±SEM. Kruskal-
886 Wallis with Dunn's post-hoc test (*$p<0.05$; **$p<0.01$; ***$p<0.001$; ****$p<0.0001$).

887 (C) Timing of ablation influences sprouting. Post-embryonic (larval) ablation of MNs
888 (CQ ∪ Is-Gal4/UAS-RPR,Gal80^{ts} shifted from 24°C to 29°C at L1) still triggers MN1
889 sprouting but less robustly than embryonic ablation (CQ ∪ Is-Gal4/UAS-RPR,Gal80^{ts}
890 raised at 29°C throughout). No sprouting occurs in control larvae maintained at 24°C.

(D) Quantification of MN1 bouton size, bouton number, axon area, and branch complexity across groups in (C). Data points represent single hemisegments. Control group: n = 6 larvae (12 hemisegments). For embryonic ablation: n = 7 larvae (14 hemisegments). Embryonic and control datasets are the same as in **Fig. 3**. For larval ablation, n = 7 larvae (13 hemisegments). Error bars: ±SEM. Kruskal-Wallis with Dunn's post-hoc test (*$p<0.05$; **$p<0.01$; ***$p<0.001$; ****$p<0.0001$).

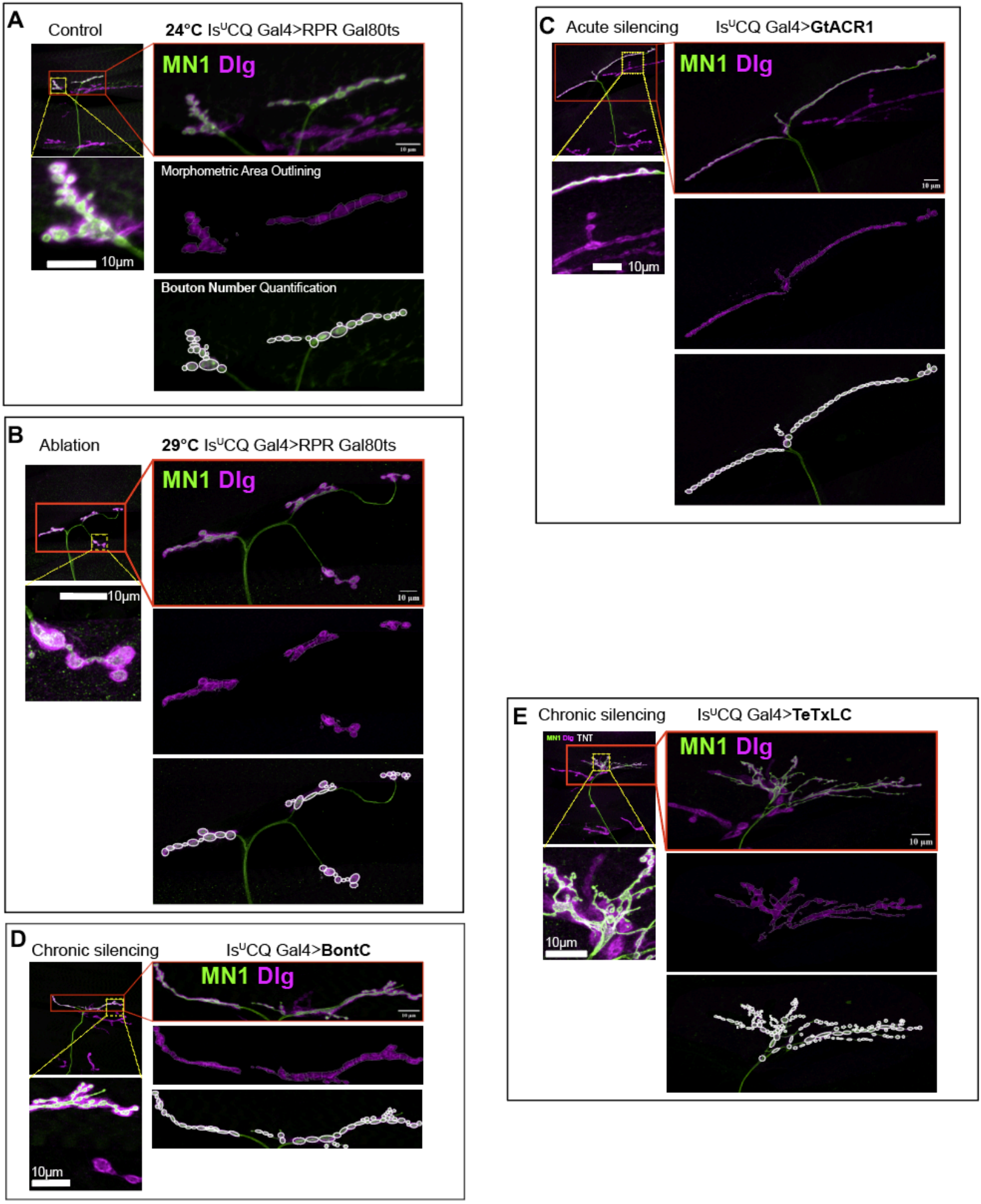
A
Control
24°C IsUCQ Gal4>RPR Gal80ts
MN1 Dlg
10µm
Morphometric Area Outlining
Bouton Number Quantification
B
Ablation
29°C IsUCQ Gal4>RPR Gal80ts
MN1 Dlg
10µm
C
Acute silencing
IsUCQ Gal4>GtACR1
MN1 Dlg
10µm
D
Chronic silencing
IsUCQ Gal4>BontC
MN1 Dlg
10µm
E
Chronic silencing
IsUCQ Gal4>TeTxLC
MN1 Dlg TNT
MN1 Dlg
10µm

957 **Fig. S1. Workflow illustrating the NMJ analysis pipeline [adapted from (41, 42)] in**
958 **different larval groups. Morphological responses of MN1 to distinct manipulations**
959 **of neighboring motor neurons.**

960 Representative images illustrate the structural remodeling of MN1 following ablation or
961 silencing of adjacent tonic and phasic motor neurons (MNs), as visualized with
962 membrane-targeted GFP and Dlg immunostaining.

963 **(A)** In temperature-controlled **unmanipulated controls** (CQ ∪ Is-Gal4 > UAS-RPR,
964 Gal80ts; raised entirely at 24°C), MN1 displays its typical morphology, forming a
965 compact NMJ exclusively on its native target, Muscle 1. No ectopic projections or
966 abnormal branching are detected.

967 **(B)** In the **ablation group** (CQ ∪ Is-Gal4 > UAS-RPR, Gal80ts; raised at 29°C),
968 selective apoptosis of neighboring MNs induces a dramatic response in MN1. The axon
969 extends beyond its native territory and establishes new, ectopic NMJs on denervated
970 Muscles 2, 9, and 10, demonstrating robust sprouting and target reinnervation.

971 **(C)** In the **acute silencing condition** (CQ ∪ Is-Gal4 > UAS-GtACR1; light-exposed),
972 MN1 remains restricted to Muscle 1. Although NMJ area and bouton number are
973 elevated relative to controls, MN1 does not form branches onto adjacent muscles.

974 **(D)** In the **chronic silencing group targeting both evoked and spontaneous release**
975 (CQ ∪ Is-Gal4 > UAS-BoNT-C), MN1 similarly exhibits increased bouton numbers but no
976 ectopic sprouting. The NMJ remains confined to its native muscle target, and axon
977 branching remains limited.

978 **(E)** In the **chronic silencing group that blocks only evoked transmission** (CQ∪Is-
979 Gal4 > UAS-TeTxLC), MN1 shows the most extensive remodeling without sprouting.
980 NMJ area, bouton number, and terminal branching complexity are all significantly
981 increased compared to controls and other silencing groups. However, bouton size is
982 notably reduced. Importantly, the tonic and phasic MNs targeted by TeTxLC appear
983 morphologically normal (white arrows), suggesting that structural changes in MN1 are
984 not due to degeneration of neighboring neurons but rather reflect a plastic response to
985 altered circuit activity.

986 Scale bars and genotype-specific labeling are provided in each panel. This figure
987 complements the quantitative analysis shown in **main Figure 3**.

988